The Angola Low: relationship with southern African rainfall and ENSO.

Julien Crétat, Benjamin Pohl, Bastien Dieppois, Ségolène Berthou, Julien Pergaud

▶ **To cite this version:**

Julien Crétat, Benjamin Pohl, Bastien Dieppois, Ségolène Berthou, Julien Pergaud. The Angola Low: relationship with southern African rainfall and ENSO.. Climate Dynamics, 2019, 52 (3-4), pp.1783-1803. 10.1007/s00382-018-4222-3 . hal-02078411

HAL Id: hal-02078411
https://hal.science/hal-02078411v1

Submitted on 12 Feb 2025

HAL is a multi-disciplinary open access archive for the deposit and dissemination of scientific research documents, whether they are published or not. The documents may come from teaching and research institutions in France or abroad, or from public or private research centers.

L'archive ouverte pluridisciplinaire **HAL**, est destinée au dépôt et à la diffusion de documents scientifiques de niveau recherche, publiés ou non, émanant des établissements d'enseignement et de recherche français ou étrangers, des laboratoires publics ou privés.

The Angola Low: relationship with southern African rainfall and ENSO

Julien Crétat[1,2,*], Benjamin Pohl[2], Bastien Dieppois[3, 4, 5], Ségolène Berthou[6], Julien Pergaud[2]

1 Sorbonne Universités (UPMC, Univ Paris 06)-CNRS-IRD-MNHN, LOCEAN Laboratory, IPSL, Paris, France
2 Centre de Recherches de Climatologie, UMR 6282 Biogéosciences, CNRS/Université de Bourgogne Franche-Comté, Dijon, France
3 Centre for Agroecology, Water and Resilience, Coventry University, Coventry, UK
4 African Climate and Development Initiative, University of Cape Town, Cape Town, Republic of South Africa
5 Department of Oceanography, MARE Institute, University of Cape Town, Cape Town, Republic of South Africa
6 Met Office, Hadley Centre, Exeter, United Kingdom

Submitted to Climate Dynamics

09/01/2017

Revised

21/02/2018
23/04/2018

Accepted
24/04/2018

*Correspondence to:
Julien Crétat, Laboratoire d'Océanographie et du Climat: Expérimentations et approches numériques, Boîte 100 - 4, place Jussieu 75252 PARIS Cedex 05.
E-mail: julien.cretat@locean-ipsl.upmc.fr

Abstract

The main states of the Angola Low (AL) are identified using clustering analysis applied to daily anomalous patterns of 700-hPa wind vorticity over Angola and adjacent countries from November to March for the 1980/81–2014/15 period. At the daily timescale, we examine the extent to which the main states of the AL modulate daily rainfall over southern Africa. At the interannual timescale, we assess both the relationship between the occurrence of these AL states and El Niño Southern Oscillation (ENSO) and the role of the AL in explaining ENSO's failure in driving southern African rainfall at times. Three reanalyses are considered to account for uncertainties induced by the scarcity of data available for assimilation over southern Africa.

Three preferential states of the Angola Low are identified: AL state close to its seasonal climatology with slight zonal displacements, anomalously weak AL state and anomalously strong AL state with meridional displacements. These different states all significantly modulate daily southern African rainfall. Near-climatological AL state promotes wet rainfall anomalies over eastern subtropical southern Africa and dry rainfall anomalies over its western part. A slight westward shift in the near-climatological position of the AL leads to reversed zonal gradient in rainfall. The remaining regimes significantly modulate the meridional gradient in southern African rainfall. Anomalously weak and anomalously northward AL states promote wet rainfall anomalies over tropical southern Africa and dry rainfall anomalies over subtropical southern Africa. The reverse prevails for anomalously southward AL.

At the interannual timescale, ENSO significantly modulates the seasonal occurrence of most AL states in the three reanalyses. Anomalously weak and southward AL states are more strongly correlated with regional rainfall than ENSO in all reanalyses, suggesting that accounting for AL variability may improve seasonal forecasts. Case study analysis of the major 1982/83 and 1997/98 El Niño events suggests that the weak rainfall anomalies and strong seasonal AL in 1997/98 may result from counteracting effects between ENSO and Indian Ocean coupled modes of variability.

Keywords: Angola Low – clustering analysis – daily rainfall – ENSO – interannual variability – southern Africa

1. Introduction

Extending from the tropics to the mid-latitudes and flanked by the South Atlantic and South Indian oceans, southern Africa (south of 10°S) is a semi-arid region highly vulnerable to climate variability, especially to rainfall due to the societal dependence of rain-fed agriculture. Rainfall mostly occurs from November to March (NDJFM) and experiences significant year-to-year variability. El Niño Southern Oscillation (ENSO) is the main driver of southern African rainfall variability at the interannual timescale (*e.g.* Ropelewski and Halpert 1989; Lindesay 1988; Rouault and Richard 2005; Crétat et al. 2010; Ratna et al. 2013; Ratnam et al. 2014; Dieppois et al. 2015). Overall, southern Africa receives below normal seasonal rainfall amounts during El Niño events, and reversely during La Niña events. However, ENSO fails at explaining seasonal rainfall anomalies at times (Lyon and Mason 2007; Fauchereau et al. 2009; Hoell et al. 2015, 2017). For instance, near normal seasonal rainfall amounts were recorded over southern Africa during the exceptionally strong El Niño event of 1997/98 (Lyon and Mason 2007).

In austral summer, earlier studies primarily focused on eastward propagating tropical-temperate troughs (D'Abreton 1992; Todd and Washington 1999; Washington and Todd 1999; Todd et al. 2004; Fauchereau et al. 2009; Hart et al. 2010; Ratna et al. 2013; Vigaud et al. 2012; Macron et al. 2014) since they provide abundant rainfall over southern Africa. By contrast, the Angola Low (AL) has received much less attention despite it also significantly impacts on southern African rainfall (Mulenga 1998; Cook et al. 2004; Reason and Jagadheesha 2005; Munday and Washington 2017). The AL is a low-pressure system centered at about 17°S over the Bié plateau in central Angola. The AL develops from October to March and has long been considered as a heat low driven by dry convection processes and associated surface heating (Mulenga 1998). Using both reanalyses and global climate models,

Munday and Washington (2017) demonstrated that the heat low moves southward over the Kalahari during the core of austral summer, while cyclonic vorticity remains over Angola through moist processes reminiscent of tropical lows. They also pointed out the role of the AL in explaining the model spread in simulating seasonal rainfall amounts along a northwest–southeast band extended from Angola down to the Mozambican Channel. These results call thus for better understanding of the influence of the AL on regional rainfall.

How the AL may impact southern African rainfall has been partly addressed in the literature. At the seasonal timescale, the more intense the AL is, the larger summer rainfall amounts are over southern Africa (Cook et al. 2004). At the intraseasonal timescale, intensification of the AL favours wet spells over South Africa, southern Angola and southern Namibia (Rouault et al. 2003; Cook et al. 2004; Reason and Jagadheesha 2005; Hermes and Reason 2009). The AL influences regional rainfall variability by modulating easterly and northeasterly wind anomalies from the southwestern tropical Indian Ocean and the Congo Basin, respectively, and westerly wind anomalies from the tropical Atlantic (Rouault, 2003; Cook et al., 2004; Vigaud et al. 2007, 2009; Hermes and Reason, 2009). At the interannual timescale, the AL has been suggested to be partially independent from ENSO. Some El Niño years are associated with weak AL and reduced moisture convergence over southern Africa (Cook 2000), while some others are not (Lyon and Mason 2007). This suggests that the AL plays a role in explaining the failure of ENSO in driving southern African rainfall variability at times.

The present study aims at revisiting the influence of the AL on southern African rainfall and its interannual relationship with ENSO based on the identification of its main states at the daily timescale in three modern reanalyses. The questions addressed in this study are twofold:

(i) At the daily timescale, how does the AL influence southern African rainfall

patterns?

(ii) At the interannual timescale, does the AL co-vary with ENSO and can the AL explain southern African rainfall variability beyond ENSO?

This paper is organized as follows. Section 2 presents the three reanalyses and the methodology used for identifying the main AL states at the daily timescale. Section 3 presents associated daily mean circulation and rainfall anomalies. Section 4 focuses on the interannual relationship between the AL states and both ENSO and seasonal southern African rainfall. Section 5 gives the main conclusions.

2. Datasets and methodology

2.1 Datasets

Three reanalyses are used to examine the spatio-temporal variability of the AL at the daily timescale for the NDJFM 1980/81–2014/15 period: the National Center for Environmental Prediction-Department of Energy reanalysis version 2 (NCEP2; Kanamitsu et al. 2002), the European Centre for Medium-Range Forecasts Interim Reanalysis (ERA-I; Dee et al. 2011) and the Modern Era Retrospective-analysis for Research and Applications version 2 (MERRA2; Gelaro et al. 2017). These reanalyses differ in many ways, including horizontal and vertical resolution, data assimilation technique and sea surface temperature (SST) forcing (Table 1). Their joint analysis allows accounting for uncertainties due to such model settings in a region where observations available for assimilation are sparse, even during the satellite era. The main atmospheric fields used here are horizontal winds at 700-hPa and their relative vorticity, together with velocity potential at 200-hPa. These are class-A variables (that is,

157 directly constrained by the assimilated observations).

158

159 We also use two rainfall datasets to assess how the AL influences southern African rainfall.
160 At the local scale (*i.e.* grid point), the one-degree daily precipitation data version 1.2 of the
161 Global Precipitation Climatology Project (GPCP; Huffman et al. 2001; Huffman and Bolvin
162 2012), available from October 1996-onward, has been selected. The GPCP data is used to
163 examine the daily mean anomalous rainfall patterns associated with the main states of the AL
164 for the overlapping period (NDJFM 1996/97–2014/15). At the regional timescale, we use the
165 Summer Rainfall Index (SRI; Dieppois et al. 2016) to analyze the interannual relationship
166 between the seasonal occurrence of the AL and NDJFM rainfall over subtropical southern
167 Africa. The SRI is derived over the 1980/81–2011/12 period from the 0.5° x 0.5° monthly
168 rainfall of the Climatic Research Unit dataset version 3.23 (CRU TS3.23; Harris et al. 2014).
169 The SRI is defined as rainfall amounts area-averaged over all grid points within subtropical
170 southern Africa, south of 20°S, where austral summer rainfall is predominant (Dieppois et al.
171 2016).

172

173 The Hadley Centre Sea Ice and SST version 1.1 dataset (HadISST; Rayner et al. 2003) is used
174 to examine the relationship between ENSO and the seasonal occurrence of the AL states at
175 the interannual timescale. The HadISST data provides monthly SSTs on a 1° x 1° grid from
176 1871-onward and is also used to derive a proxy for ENSO variability based on boreal winter
177 (December-January) SSTs area-averaged in the Niño3.4 region (5°S-5°N; 170°W-120°W).

178

179 *2.2 Methodology*

180

181 *2.2.1 Clustering procedure*

182

183 The Agglomerative Hierarchical Clustering (AHC; Gong and Richman 1995) procedure is
184 used to identify the main states of the AL. The AHC is a bottom-up clustering approach
185 providing a hierarchy of partitions of the spatio-temporal variability of a given parameter. The
186 AHC classifies either the temporal variability of spatial patterns or the spatial variability of
187 local time-series. The AHC consists in a step-by-step merging of *N* spatial patterns or *N* time-
188 series into *N*-to-1 clusters of size 1-to-*N* according to their spatial or temporal similarity.

189

190 Figure 1 provides a schematic view of the AHC procedure for *N*=5 spatial patterns of a given
191 parameter described by two grid points A and B. In the first step (Fig. 1a), the *N*=5 spatial
192 patterns constitute *N*=5 initial clusters. A dissimilarity matrix D is computed between all pairs
193 of initial clusters (*i.e.* 10 combinations for *N*=5). The Euclidean distance is used to quantify
194 dissimilarity and is defined as follows between two initial clusters *i* and *j*:

195 $$d_{ij} = \sqrt{(A_i - A_j)^2 + (B_i - B_j)^2} \quad Eq(1),$$

196 The Euclidean distance in Eq(1) is computed 10 times for *N*=5 and stored in D. In the second
197 step (Fig. 1b), the two initial clusters having the smallest Euclidean distance d_{ij} are merged to
198 form a new cluster *k* of size $n_k = n_i + n_j$ (n_k=2 in Fig. 1b). A new set of distances d_{km} is then
199 computed between the centroid of cluster *k* and the *m* remaining clusters as follows:

200 $$d_{km} = \alpha_i d_{im} + \alpha_j d_{jm} + \beta d_{ij} \;\; Eq(2).$$

201 The coefficients α_i, α_j and β force the centroid of cluster *k* to minimize intra-cluster variance
202 according to the Ward's method (1963). These coefficients are given by:

203 $$\alpha_i = \frac{n_i + n_m}{n_k + n_m}, \alpha_j = \frac{n_j + n_m}{n_k + n_m}, \beta = \frac{-n_m}{n_k + n_m} \quad Eqs(3, 4\ and\ 5).$$

204 The dissimilarity matrix D is then updated by replacing the d_{im} and d_{jm} distances by the d_{km}
205 distances. The agglomerative partitioning continues until the *N*=5 spatial patterns are merged

206 into a unique cluster (Fig. 1c-e).

207

208 The AHC procedure does not explicitly give an optimal number of clusters to be retained, but
209 allows multiple partitionings depending on the degree of details expected. The dendrogram
210 (Fig. 1a-e; right column) shows the evolution of intra-class heterogeneity at each step of the
211 clustering, and can be used to select the appropriate number of clusters to be retained.
212 Contrary to Empirical Orthogonal Function, the AHC does not suppose any orthogonality,
213 which has two consequences. First, artificial north-south or west-east structures are not
214 imposed "by construction". Second, the AHC allows exploring non-linearities and robustness
215 of a given cluster by splitting it into sub-clusters of smaller size. The AHC procedure has
216 been successfully used to explore rainfall and atmospheric spatio-temporal variability (*e.g.*
217 Crétat et al. 2010, 2015; Pohl and Camberlin 2014).

218

219 *2.2.2 Clustering settings*

220

221 Prior to apply the AHC, a reasonable proxy of the AL is selected based on the examination of
222 the mean atmospheric circulation at 850- and 700-hPa in austral summer (Fig. 2). Three
223 regional lows appear clearly over southern Africa: a heat low over the Kalahari and two
224 tropical lows over the Mozambique Channel and Angola. The heat low is characterized by
225 shallow convection. Cyclonic winds and negative vorticity at 850-hPa (Fig. 2a-c) oppose
226 anticyclonic winds and positive vorticity at 700-hPa (Fig. 2d-f). The two tropical lows have
227 larger vertical extension, as illustrated by persistent cyclonic vorticity at 700-hPa (Fig. 2d-f).
228 While these three regional features emerge in all reanalyses, important differences are found
229 in the low-levels. The 850-hPa mean circulation pattern is smoothed in the coarse resolution
230 NCEP2 (Fig. 2a), while it is noisier spatially in ERA-I and MERRA2 (Fig. 2b-c). In

mountainous regions, the surface often peaks above the 850-hPa geopotential height, which prevents using this level to portray the AL variability in the two highest-resolution reanalyses. The mean vorticity pattern over Angola and adjacent countries is also more consistent between the three reanalyses at 700-hPa than 850-hPa (Fig. 2a-f). For these reasons, this parameter at this level is chosen as a proxy of the AL in the three reanalyses.

The mean 700-hPa vorticity over southern Africa together with its interannual variability (Fig. 2g-i) provide guidance for selecting the spatial domain to monitor the AL variability. The three regional lows discussed above all show substantial interannual variability. Hence, the spatial domain should be small enough to extract the variability of the AL only, with no interference from the Kalahari Low and Mozambique Channel Low. In the end, the AHC is thus applied to daily anomalies of 700-hPa vorticity in the 5°-20°S–12°-25°E region (black box in Fig. 2) over the period NDJFM 1980/81–2014/15.

2.2.3 Cluster partitioning

Figure 3 illustrates how daily patterns of 700-hPa vorticity anomalies are grouped into statistically robust AL states. First, reanalysis dependency in the magnitude of the spatio-temporal variability of the AL is evident (see total accumulated dissimilarity distance at the top of the dendrograms in Fig. 3). The variability of the AL is sharply damped in the NCEP2 compared to the two remaining reanalyses, consistent with Fig. 2g-i. This indicates that the AL variability is very sensitive to model settings (*e.g.* resolution, physical parameterization and assimilation technique).

Fig. 3 also indicates that the greatest increase in the accumulated dissimilarity distance is found when merging the two last clusters at the top of the dendrograms. These two clusters are noted regimes A and B hereafter. Merging regime A with regime B increases the dissimilarity distance by 200% in NCEP2, 15% in ERA-I and 35% in MERRA2. Such jumps in the dissimilarity distance indicate that regimes A and B refer to very different states of the AL and suggest thus that the AL variability can, at first, be divided into two main states. This is especially true for NCEP2, while there is much more diversity in both ERA-I and MERRA2, as demonstrated by many abrupt jumps in the accumulated dissimilarity distance in the 10 last merges (Fig. 3e-f).

In this study, we first present results with a partitioning into two regimes (A and B), and then into six sub-regimes for NCEP2 and ERA-I and seven sub-regimes for MERRA2. This double partitioning approach allows exploring complementary features of the AL. The 2-regime partitioning provides a symmetric view of the AL corresponding to its strong and weak phases. The 6/7-regime partitioning provides a regional view of different locations of the AL. According to the dendrograms (Fig. 3a-c), regime A splits into 4 regimes (A1 to A4) in NCEP2, 2 regimes (A1 and A2) in ERA-I and 5 regimes (A1 to A5) in MERRA2. Similarly, regime B splits into 2 regimes (B1 and B2) in NCEP2 and MERRA2 and 4 regimes (B1 to B4) in ERA-I. The size of each regime is shown in Table 2. Even in the 6/7-regime partitioning, some regimes remain very frequent (A1 and B1 in NCEP2, B1 and B3 in ERA-I, and A3 and B1 in MERRA2: Table 2).

2.2.4 Assessing statistical significance

279 The different states of the AL and their implication for southern African rainfall are examined
280 by averaging all daily anomalous patterns ascribed to each regime. The first step to evaluate
281 their robustness is to assess the representativeness of the daily mean anomalous patterns
282 associated with each regime. To that end, spatial correlations are computed between all daily
283 anomalous patterns of 700-hPa vorticity in the 5°-20°S–12°-25°E region (the input data for
284 the AHC clustering) and the average anomalous pattern of each regime. Results are
285 summarized in Figure 4. Most daily patterns are significantly correlated at the 95%
286 confidence level with the mean anomaly pattern of their corresponding regime (Fig. 4), even
287 with a 2-regime partitioning. This demonstrates that intra-regime variability is lower than
288 inter-regime variability, and thus that the mean anomalous patterns are robust.
289
290 The second step to evaluate the robustness of the AL states is to test the statistical
291 significance of the mean anomalous patterns of atmospheric circulation and rainfall associated
292 with each regime. The statistical confidence is assessed at the grid-point scale using a
293 bootstrapping approach at the 95% confidence level. For a given regime, 1000 surrogates of *n*
294 daily anomaly patterns are randomly extracted, with *n* corresponding to 25% of the size of the
295 regime. The *n* daily anomalous patterns are averaged to generate 1000 mean anomalous
296 patterns and to determine the 95% confidence level.
297
298 The third step is to discuss the sensitivity of the results according to the parameter, the level
299 and the domain used to infer the AL states. Preliminary tests indicate that surface pressure and
300 700-hPa geopotential height lead to little diversity in associated circulation and rainfall
301 anomalies. Corresponding regimes are mostly driven by mid-latitude circulation (Fig. S1).
302 The mean circulation and rainfall anomalies are qualitatively similar when the AHC is applied
303 to 600-hPa, 700-hPa and 775-hPa vorticity anomalies (Figs. S2-3). Results are more sensitive

304 to the domain size (Figs. S4-5). Increasing the domain size towards the East or South leads to
305 deep modifications of some regimes. These differences could be due to the influence of the
306 Mozambique Channel Low east of the AL and the Kalahari Low and mid-circulation south of
307 it, interfering with the canonical AL.
308
309
310 **3. Daily mean circulation and rainfall**
311
312 This section characterizes the main AL states (anomalous circulation patterns on the
313 horizontal, vertical structure), and their relationship with daily rainfall patterns over southern
314 Africa.
315
316 *3.1 Binary view of the Angola Low*
317
318 The mean anomalous patterns of regimes A and B are shown in Fig. 5 for 700-hPa
319 atmospheric circulation and in Fig. 6 for rainfall. In all reanalyses, regime A depicts
320 significant cyclonic vorticity and wind anomalies over Angola and anticyclonic vorticity and
321 wind anomalies poleward (Fig. 5a-c). Regime A thus describes anomalously strong AL.
322 Associated rainfall anomalies are wet southeast of the cyclonic vortex and dry north of it (Fig.
323 6a-c). Circulation and rainfall anomalies associated with regime B (Figs. 5d-f and 6d-f) are
324 almost opposite to those of regime A (Figs. 5a-c and 6a-c). Regime B describes thus
325 anomalously weak AL. Both significance and amplitude of the anomalies associated with
326 these two AL states are strongly reanalysis-dependent (Figs. 5-6). Anomalies are more
327 significant in regime A for ERA-I and in regime B for NCEP2 and MERRA2. This could be

328 due to sampling errors, which are larger for NCEP2 and MERRA2 than for ERA-I in regime
329 A, and reversely in regime B (Fig. 4).
330
331 The vertical structure of the AL is examined through cross-sections of vorticity and wind
332 anomalies averaged between 12°E and 25°E (Fig. 7). Results are only shown for regime A,
333 which corresponds to a strong AL. The vertical structure of regime B is similar to regime A
334 but with anomalies of opposite sign (not shown). Although daily mean anomalies are stronger
335 in ERA-I than in NCEP2 and MERRA2, the vertical cross-sections are consistent regardless
336 the reanalysis. A tripole vorticity pattern extends in the whole troposphere from 30°S to 5°S,
337 with greatest anomalies between 850- and 400-hPa (Fig. 7a-c). Vorticity anomalies are
338 cyclonic between 25°S and 15°S and anticyclonic poleward. These anomalies depict sharp
339 horizontal wind shear between strong and significant westerly wind anomalies centered at
340 15°S and significant easterly anomalies further south (Fig. 7d-f). The AL is shown to control
341 not only lower-layer moisture fluxes, but also mass fluxes in the middle and upper
342 troposphere.
343
344 *3.2 Refined view of the Angola Low*
345
346 The binary view of the AL is useful to discuss its basic characteristics. However, sampling
347 errors remain large (Fig. 4), calling for a more detailed decomposition of the AL variability.
348 Partitioning into 6/7-regimes substantially refines the above analyses, especially in ERA-I and
349 MERRA2 (Fig. 4). Figures 8 and 9 show corresponding daily mean composite anomalies in
350 700-hPa atmospheric circulation and rainfall, respectively.
351

For conciseness, the main states of the AL are gathered into three groups based on the similarity in the mean anomalous patterns of circulation and rainfall of the 6/7 regimes. The first group is composed of regimes B1 and B2 in all reanalyses (Figs. 8a-f and 9a-f). Regime B1 occurs 20% to 36% of the time depending on the reanalysis and is more frequent than regime B2 (Table 2). The mean anomalous circulation pattern of regime B1 (Fig. 8a-c) is similar to that of regime B (Fig. 5d-f) and can be interpreted as a weak AL. Circulation anomalies associated with regime B2 (Fig. 8d-f) display a tripole anomalous pattern very similar to regime A (Fig. 5a-c) but slightly shifted northward. Thus, regime B2 describes an anomalously northward location of the AL. Interestingly, regime B2 is associated with an enhanced low over the Mozambique Channel in all reanalyses (Fig. 8d-f). These two systems favour significant westerly wind anomalies from tropical southern Africa to the western tropical Indian Ocean (Fig. 8d-f). This denotes drastically reduced moisture transport from the Indian Ocean towards southern Africa (not shown). In spite of their differences, regimes B1 and B2 are both associated with significant low-level anticyclonic circulation anomalies and dry anomalies over subtropical southern Africa (Figs. 8a-f and 9a-f).

The second group consists of regimes associated with weak anomalies over Angola and adjacent countries, denoting an AL close to its seasonal climatology (Fig. 2d-f). This group is composed of regimes A1-2 in NCEP2 and MERRA2 and B3-4 in ERA-I (Fig. 8g-l). Both the circulation anomalies and the size of these regimes largely differ from one reanalysis to another (Fig. 8g-l, Table 2). In NCEP2 and MERRA2, the circulation anomalies of regime A1 describe a slight strengthening of the climatological AL (Fig. 2d and f). The magnitude of circulation anomalies associated with regime A1 is much weaker in NCEP2 (Fig. 8g) than MERRA2 (Fig. 8i), due to larger sampling errors (Fig. 4). In ERA-I, regime B3 is the most frequent regime (30.5% of the time: Table 2) and depicts a slight but significant eastward shift

377 in the location of the AL (Fig. 8h). This shift is embedded in significant large-scale cyclonic
378 anomalies oriented in the northwest-southeast direction and extending from the southeastern
379 Atlantic at ~15°S to the southwest Indian Ocean at ~40°S. Although circulation anomalies are
380 reanalysis-dependent, regimes A1 in NCEP2 and MERRA2, as well as B3 in ERA-I, are all
381 associated with significant westerly anomalies north of the cyclonic vortex and northwesterly
382 anomalies on its eastern edge (Fig. 8g-i). Such northwesterly anomalies favour low-level
383 convergence over eastern subtropical southern Africa and low-level divergence over its
384 western part. As a result, regimes A1 in NCEP2 and MERRA2, and B3 in ERA-I, all promote
385 a significant zonal dipole in rainfall over subtropical southern Africa, with wet anomalies on
386 its eastern part and dry anomalies on the west (Fig. 9g-i). While regime B3 of ERA-I has no
387 equivalent in NCEP2 and MERRA2, its opposite phase exists in all reanalyses (regime A2 in
388 NCEP2 and MERRA2 and B4 in ERA-I; Figs. 8j-l and 9j-l). This suggests that slight zonal
389 shifts in the location of the AL may sharply modulate the zonal rainfall gradient over
390 subtropical southern Africa.
391
392 The third group represents the southernmost extension of the AL. This group is composed of
393 regimes A3-4 in NCEP2, A1-2 in ERA-I and A3-5 in MERRA2 (Figs. 8m-s and 9m-s). Most
394 of these regimes are very robust in terms of sampling errors (Fig. 4). The cyclonic vortex is
395 centered near 18°S in all cases, but its longitude is regime-dependent (Fig. 8m-s). All the
396 regimes ascribed to this group depict significant cyclonic anomalies over subtropical southern
397 Africa and significant anticyclonic anomalies over tropical southern Africa (Fig. 8m-s). This
398 results in a stronger than usual meridional gradient of rainfall over southern Africa, with wet
399 anomalies in the subtropics and dry anomalies in the tropics (Fig. 9m-s). This group is
400 recorded 17.2% of the time in NCEP2 (A3+4), 25.3% in ERA-I (A1+2) and 37.5% in
401 MERRA2 (A3+4+5; Table 2).

The vertical structure of the AL decomposed into 6/7 regimes (Fig. S6) further illustrates that the AL is not limited to the low troposphere. In particular, anomalously weak, northward and southward AL states depict significant vorticity anomalies throughout the troposphere, which are greatest above 850-hPa (Fig. S6a-c, d-f and m-s, respectively). In line with Munday and Washington (2017), the AL cannot simply be seen as a thermal low driven by surface heating and dry convection.

To summarize, a refined view of the AL helps identify three preferential states with contrasted impacts on southern African rainfall: anomalously weak AL, near-climatological state with slight zonal displacements, and anomalously strong AL with meridional displacements. Weak AL and meridional displacements significantly shape the meridional rainfall gradient between tropical and subtropical southern Africa. Near-climatological AL or its slight zonal displacements modifies the zonal rainfall gradient in subtropical southern Africa.

3.3 Synoptic context

The daily evolution of selected states of the AL is analyzed in a 9-day window to discuss the synoptic context in which they develop. The daily evolution is constructed as follows. First, all sequences of successive days ascribed to the same regime are identified. Second, the sequences lasting less than two days are removed to exclude short-lived events. Third, the first day of all sequences is averaged to form the composite at lag(0). Finally, the same procedure is performed from lag(-4) to lag(+4). This approach is designed to focus on the

427 growing and mature phases of the AL. Although Figure 10 shows the results for ERA-I only,
428 results obtained for NCEP2 and MERRA2 are discussed as well.
429
430 Circulation anomalies associated with weak AL (*i.e.* B1 in the three reanalyses) are relatively
431 stationary (Fig. 10a-e). Both easterly wind anomalies over the eastern equatorial Indian Ocean
432 and quasi-stationary cyclonic anomalies over the southeast Atlantic and southwest Indian
433 Oceans prevail during the entire developing and mature phases of weak AL (Fig. 10a-e). This
434 result is robust across the three reanalyses (not shown) and suggests large-scale control and
435 long-lasting occurrence of this frequent AL state (B1 occurs 20% to 36% of the time; Table
436 2).
437
438 Northward AL location is favoured by tropical-extratropical interactions in all reanalyses.
439 These tropical-extratropical interactions are illustrated for regime B2 in ERA-I (Fig. 10f-j). In
440 the tropics, B2 is dominated by a persistent cyclonic vortex northeast off Madagascar. This
441 cyclonic vortex is embedded in a northwest-southeast tilted band of active convection
442 reminiscent of a northeastern shift of the Intertropical Convergence Zone (Fig. 10f-g). Such a
443 cyclonic vortex promotes significant westerly wind anomalies from north of Madagascar to
444 the Congo Basin starting at lag(-4). A mid-latitude eastward propagating wave-train
445 disturbance is also seen during the growing phase of B2 (Fig. 10f-g). At lag(-4), wind
446 anomalies over the southeast Atlantic Ocean are cyclonic south of 45°S and anticyclonic
447 further north. This anomaly pattern slowly propagates eastward during the following days
448 (Fig. 10f-j). The AL intensifies at lag(-2) when the southeasterly anomalies north of the mid-
449 latitude wave-train reach tropical southern Africa (Fig. 10g). The intrusion of relatively cold
450 and dry air from the extratropics above the relatively warm and wet boundary layer of tropical
451 southern Africa favours instability and rainfall. On the other hand, such an intrusion stabilizes

452 the colder and drier lower troposphere of subtropical southern Africa and favours dry
453 conditions. Regime B2 matures at lag(0) and rapidly decays afterward, as the cyclonic vortex
454 off Madagascar weakens and the mid-latitude transient disturbance displaces over the
455 extratropical Indian Ocean (Fig. 10i-j).
456
457 The near-climatological state of the AL is described by regime B3 in ERA-I. This regime has
458 no equivalent in NCEP2 and MERRA2 in a 6/7-regime partitioning. Regime B3 relates to
459 significant circulation anomalies in the tropics throughout its life cycle (Fig. 10k-o). B3 is
460 also associated with a significant mid-latitude disturbance embedded in an eastward
461 propagative Rossby wave. Positive air-land feedback may occur, as suggested by the abrupt
462 strengthening of cyclonic anomalies over subtropical southern Africa as the disturbance
463 reaches the landmass between lag(-2) and lag(0) (Fig. 10l-m). These anomalies rapidly
464 weaken afterward as the disturbance reaches the Indian Ocean (Fig. 10n-o). The time-
465 evolution of regimes B4 in ERA-I and A2 in NCEP2 and MERRA2 is similar to that
466 described above, but with anticyclonic wind anomalies instead of cyclonic in the mid-
467 latitudes (not shown).
468
469 The life cycle of southward AL is illustrated by regime A1 in ERA-I (Fig. 10p-t) and is
470 consistent among reanalyses (not shown). As for northward AL, southward AL is associated
471 with strong tropical-extratropical interactions. Easterly wind anomalies prevail north of
472 Madagascar during the growing phase of regime A1 in response to anomalously active
473 convection over East Africa (Fig. 10p-r). At the same time, significant anticyclonic anomalies
474 develop south of South Africa (Fig. 10q-r). Regime A1 matures at lag(0) when both easterly
475 anomalies off northern Madagascar and mid-latitude anticyclonic anomalies are the most

476 pronounced (Fig. 10r). Regime A1 then rapidly weakens after lag(+2), as both convection
477 over East Africa and mid-latitude anticyclonic circulation weaken (Fig. 10s-t).
478
479 The analysis of the synoptic context of development and intensification of the AL
480 demonstrates the significant roles of tropical and mid-latitude circulation. In particular,
481 meridional displacements of the AL are favoured by tropical-extratropical interactions in all
482 reanalyses. This calls for better understanding of how tropical-extratropical interactions
483 modulate the AL variability at the daily timescale and the relationship between the AL and
484 tropical-temperate troughs.
485
486
487 **4. ENSO–Angola Low co-variability and consequences on southern African rainfall**
488
489 This section aims at assessing the influence of ENSO on the seasonal occurrence of the AL,
490 as seen by a 6/7-regime partitioning, and the possible implication of the AL for ENSO's
491 failure in driving southern African rainfall at times.
492
493 *4.1 ENSO–Angola Low co-variability*
494
495 Figure 11 presents the interannual variability of the seasonal occurrence of the main AL
496 states. Weak AL (*i.e.* B1) clearly decreases over the period (Fig. 9a-c), while the reverse
497 prevails for many regimes describing anomalously southward AL (*i.e.* A3 in NCEP2, A1 and
498 A2 in ERA-I and A4 in MERRA4; Fig. 9m-n, q, r). These trends are more pronounced in
499 NCEP2 than in ERA-I and MERRA2. Additional analyses and century-long data would be
500 required to disentangle the contribution of climate warming and decadal climate variability on

these signals. Here, we aim at assessing how the seasonal occurrence of the AL is influenced by ENSO at the interannual timescale. To that end, we compute linear correlation between the seasonal occurrence of the AL and both grid-to-grid NDJFM SSTs (Fig. 12) and December-January (DJ) SSTs of the Niño3.4 region (Table 3).

In all reanalyses, the seasonal occurrence of weak AL is positively correlated to Niño3.4 SSTs (Table 3). The correlation pattern over the Pacific also reflects the typical signature of ENSO (Fig. 12a-c). This demonstrates that anomalously weak AL occurs more frequently during El Niño years and less frequently during La Niña years. On the other hand, anomalously southward AL tends to be more frequent during La Niña years and less frequent during El Niño years (Table 3 and Fig. 12m-s). This relationship between ENSO and extreme phases of the AL is statistically less robust in NCEP2 than in ERA-I and MERRA2 (Table 3).

The influence of ENSO on the remaining AL states is more reanalysis-dependent. Northward AL is poorly correlated with ENSO and global SSTs in NCEP2 and ERA-I (Table 3 and Fig. 12d-e), while positively and significantly correlated with ENSO in MERRA2 (Table 3 and Fig. 12f). Near-climatological AL is significantly influenced by ENSO in NCEP2 and MERRA2 (Fig. 12g, i, j, l), but not in ERA-I (Fig. 12h, k). These results highlight weaker and more ambiguous influence of ENSO on the near-climatological states of the AL.

4.2 Role of the Angola Low in the complex relationship between ENSO and southern African rainfall

Over southern Africa, summer rainfall variability does not respond systematically to strong ENSO events at the interannual timescale (*e.g.* Lyon and Mason 2007; Fauchereau et al.

2009; Hoell et al. 2015, 2017). Here, we explore to which extent the AL plays a role in explaining the failure of ENSO in driving southern African rainfall variability at times.

Figure 13 presents a scatterplot between DJ SSTs of the Niño3.4 region and the NDJFM SRI over the 1980/81–2012/13 period. The SRI describes regions of southern Africa, south of 20°S, where austral summer rainfall is predominant (Dieppois et al. 2016). The correlation value between Niño3.4 SSTs and the SRI reaches -0.37 (significant at the 95% confidence level: Fig. 13). El Niño events tend to promote dry conditions over subtropical southern Africa, as opposed to La Niña events, hereby corroborating many previous studies (*e.g.* Ropelewski and Halpert 1989; Lindesay 1988; Rouault and Richard 2005; Crétat et al. 2010; Ratna et al. 2013; Ratnam et al. 2014; Dieppois et al. 2015). Even through this relationship is statistically significant, ENSO explains only about 13% of the SRI interannual variability. This low value indicates that near-climatological conditions can also occur during El Niño or La Niña years. For instance, six out of the 33 seasons analyzed here are wetter than normal during El Niño-like years (Fig. 13: top-right corner).

Figure 14 helps discuss the potential role of the AL in explaining residual SRI variability over the 1980/81–2012/13 period. In all reanalyses, the seasonal occurrence of the two extreme phases of the AL (*i.e.* anomalously weak and anomalously southward phases) is much more strongly correlated with the SRI (Fig. 14a-c, m-s) than with ENSO (Table 3). Moreover, the correlation between the two extreme phases of the AL and the SRI are generally larger than those between ENSO and the SRI. This suggests that, regardless the influence of ENSO, extreme phases of the AL may improve seasonal rainfall predictability over subtropical southern Africa. Better understanding of the specific influence of the extreme phases of the

AL on the interannual variability of subtropical southern African rainfall requires partial decoupling experiments with ENSO removed (*e.g.* Terray et al. 2016; Crétat et al. 2016).

The role of the remaining states of the AL in interfering the ENSO–SRI relationship is not clear in NCEP2 (Fig. 14b,g,j) and ERA-I (Fig. 14e,h,k). However, in MERRA2, both anomalously northward (Fig. 14f: B2) and near-climatological AL with slight westward shift (Fig. 14l: A2) are more strongly correlated with the SRI than ENSO, further suggesting that they could modulate ENSO effects on southern African rainfall.

4.3 Case study of contrasted El Niño impacts on southern African rainfall

The very strong 1997/98 El Niño, which was associated with near-climatological rainfall over subtropical southern Africa, is here compared to the 1982/83 El Niño, which led to extremely dry conditions (Fig. 13). Lyon and Mason (2007) suggest that the 1997/98 El Niño was associated with an anomalously strong AL, which could have interfered with the forcing of ENSO regionally. Our regime approach at the daily timescale corroborates this seasonal result by showing that weak AL was more frequent than normal in 1982/83, while less frequent than normal in 1997/98 (Fig. 14a-c), regardless the reanalysis.

The large-scale climate background conditions during the two contrasted El Niño events are documented in Figure 15 to further understand why weak AL is less frequent in 1997/98 than in 1982/83. Both events are associated with SST warming in the eastern equatorial Pacific Ocean and SST cooling in its western tropical part (Fig. 15a-c). This zonal SST gradient is associated with an eastward shift in the mean Walker circulation over the tropical Pacific during both events (Fig. 15d-f), with anomalous upper-level convergence over the western

575 Pacific Ocean and anomalous upper-level divergence over the eastern Pacific Ocean. These
576 SST and upper-level circulation anomalies are accompanied by equatorial westerly wind
577 anomalies in the lower troposphere (Fig. 15d-f).
578
579 Climate background conditions associated with the 1982/83 and 1997/98 El Niño events
580 differ in other regions. In 1982/83, cold SST conditions prevail in almost the whole Atlantic
581 (Fig. 15b), with anomalous 200-hPa convergence east of 0° and anomalous 200-hPa
582 divergence west of 0° (Fig. 15e). This upper-level circulation dipole is associated with a
583 strengthening of the South Atlantic High, favouring clear-sky conditions and local SST
584 warming (Fig. 15b). Strengthening of the South Atlantic High promotes low-level
585 southeasterly wind anomalies over southern Africa, hence unfavourable background
586 conditions for the development of the AL (Fig. 15e). On the other hand, warm SST anomalies
587 prevail in the whole tropical Atlantic in 1997/98 (Fig. 15c) and the South Atlantic High is
588 anomalously weak (Fig. 15f). In addition, the zonal gradient in 200-hPa velocity potential
589 anomalies sharply differs in 1997/98 compared to 1982/83. The 1997/98 zonal gradient
590 opposes anomalous upper-level divergence over Africa to anomalous upper-level
591 convergence over and east of the eastern Indian Ocean (Fig. 15f). This is accompanied by
592 strong easterly wind anomalies along the equator in the low levels and by a mid-latitude
593 disturbance southeast of Madagascar (Fig. 15f).
594
595 Over the Indian Ocean, a negative Subtropical Indian Ocean Dipole (SIOD; Behera and
596 Yamagata 2001) is seen in both 1982/83 and 1997/98. In 1982/83, the negative SIOD is
597 located off Australia and poorly connects with the tropical Indian Ocean (Fig. 15b). In
598 1997/98, the negative SIOD is located southeast of Madagascar and is strongly connected
599 with the tropical Indian Ocean (Fig. 15c). Tropical Indian Ocean SSTs show a positive Indian

600 Ocean Dipole (IOD; Saji et al. 1999) in 1997/98 only, with cool SSTs in its eastern equatorial
601 part and warm SSTs in its western tropical part (Fig. 15c). Such a positive IOD promotes
602 anomalously active convection over East Africa and the western tropical Indian Ocean as well
603 as significant 850-hPa westerly wind anomalies over tropical southern Africa (Fig. 15f),
604 hence favourable background conditions for the development of the AL.
605
606 Hoell et al. (2017) show that the SIOD strengthens the ENSO-related atmospheric response
607 over southern Africa when these two modes of variability are in opposite phases. The case of
608 the 1997/98 El Niño does not support their findings, suggesting that the position of the SIOD
609 and/or the SIOD-IOD transitions might also be crucial in explaining the role of the AL in
610 interfering with the ENSO–southern African rainfall relationship. This hypothesis could be
611 tested through numerical experiments with partial ocean-atmosphere decoupling with
612 ENSO/IOD removed over the tropical Pacific/Indian Ocean (*e.g.* Terray et al. 2016; Crétat et
613 al 2016). Internal atmospheric variability could also play an important role for explaining the
614 AL variability. Untangling the role of SST forcing and internal atmospheric on the AL
615 variability could be examined through large ensembles of atmospheric model simulations.
616
617
618 **5. Conclusion**
619
620 This study aims at examining the Angola Low (AL) based on the Agglomerative Hierarchical
621 Clustering technique applied to the spatio-temporal variability of the daily circulation (700-
622 hPa vorticity) over Angola and adjacent countries over the NDJFM 1980/81–2014/15 period.
623 Emphasis is given on the impact of the main states of the AL on southern African rainfall
624 patterns and on the potential implication of the AL in the complex relationship between

ENSO and southern African rainfall. Three reanalyses (NCEP2, ERA-I and MERRA2) are considered to account for uncertainties.

The clustering technique allows extracting different degrees of details of the AL. Partitioning into 2 regimes depicts the opposite phases of the AL, but over-simplifies its spatio-temporal variability. A refined view of the AL into 6 or 7 regimes (depending on the reanalyses) demonstrates three main states of the AL that are robust across the reanalyses: anomalously weak AL, near-climatological state with slight zonal shifts and anomalously strong AL with meridional shifts. The influence of these different AL states on southern African rainfall is very strong. Both weakening and meridional displacements of the AL significantly impact the meridional rainfall gradient between tropical and subtropical southern Africa. A near-climatological AL or slight eastward/westward shifts significantly modulate the zonal rainfall gradient of subtropical southern Africa. All reanalyses and most AL states suggest a strong impact of both tropical and mid-latitude circulation on the AL development at the synoptic scale. This result questions the statistical significance of the role of the AL in favouring the development of tropical-temperate troughs suggested by previous studies (Cook et al. 2004; Hart et al. 2010; Macron et al. 2014). Weak and southernmost AL states appear to be the most robust features from one reanalysis to another in terms of occurrence and anomalous patterns of circulation and rainfall. However, near-climatological states of the AL are highly reanalysis dependent, suggesting that model settings (*e.g.* resolution, physics and assimilation schemes) have major impacts on the AL in a data-scarce region.

At the interannual timescale, the two extreme phases of the AL (*i.e.* the anomalously weak and southward phases) show significant relationships with ENSO. Weak AL is more frequent during El Niño years, and southward AL during La Niña years. The influence of ENSO on the

interannual variability of the remaining AL states is highly reanalysis dependent, calling for cautious interpretation. Interestingly, the two extreme phases of the AL are more strongly correlated with subtropical southern African rainfall than with ENSO. This result could indicate that the two extreme states of the AL can be favoured by additional large-scale coupled modes of variability. Detailed analysis of the strong 1982/83 and 1997/98 El Niño events suggest that Indian Ocean coupled modes of variability may counteract ENSO effects on the AL.

This study demonstrates a significant and major role of the AL in modulating the spatial distribution of rainfall over both tropical and subtropical southern Africa. Additional work is now required to further understand the mechanisms influencing the intraseasonal and interannual variability of the AL, both in terms of intensification and spatial location. Sensitivity experiments using partial coupling strategy are also required to further understand the role of regional coupled modes of variability on the AL in both the presence and absence of ENSO.

Acknowledgments

We gratefully acknowledge the NOAA/OAR/ESRL PSD, ECMWF and MDISC for making available the NCEP2, ERA-I and MERRA2 reanalysis data. GPCP and HadISST data were provided by NOAA/OAR/ESRL PSD and MetOffice website, respectively. Calculations were performed using HPC resources from PSIUN-CCUB, université de Bourgogne. We also thank the two anonymous reviewers for their constructive comments.

674 **References**

675

676 Behera SK, T Yamagata (2001) Subtropical SST dipole events in the southern Indian Ocean.
677 Geophys Res Lett 28:327–330

678 Cook KH (2000) The South Indian Convergence Zone and interannual rainfall variability over
679 southern Africa. J Clim 13(21):3789–3804

680 Cook C, CJC Reason, BC Hewitson (2004) Wet and dry spells within particularly wet and dry
681 summers in the South African summer rainfall region. Clim Res 26(1):17–31

682 Crétat J, Y Richard, B Pohl, M Rouault, CJC Reason, N Fauchereau (2010) Recurrent daily
683 rainfall patterns over South Africa and associated dynamics during the core of the austral
684 summer. Int J Climatol 32:261–273

685 Crétat J, B Pohl, C Chateau Smith, N Vigaud, Y Richard (2015) An original way to evaluate
686 daily rainfall variability simulated by a regional climate model: the case of South African
687 austral summer rainfall. Int J Climatol 35:2485–2502

688 Crétat J, P Terray, S Masson, KP Sooraj, MK Roxy (2016) Indian Ocean and Indian summer
689 monsoon: relationships without ENSO in ocean-atmosphere coupled simulations. Clim
690 Dyn 49:1429–1448

691 D'Abreton P (1992) The dynamics and energetics of tropical temperate troughs over southern
692 Africa. Dissertation, University of Witwatersrand, Johannesburg, South Africa.

693 Dee DP, et al. (2011) The ERA-Interim reanalysis: configuration and performance of the data
694 assimilation system. Q J R Meteorol Soc 137:553–597

695 Dieppois B, M Rouault, M New (2015) The impact of ENSO on southern African rainfall in
696 CMIP5 ocean atmosphere coupled climate models. Clim Dyn 45:2425–2442

697 Dieppois B, B Pohl, M Rouault, M New, D Lawler, N Keenlyside (2016) Interannual to
698 interdecadal variability of winter and summer southern African rainfall, and their
699 teleconnections. J Geophys Res Atmos 121:6215–6239
700 Fauchereau N, B Pohl, CJC Reason, M Rouault, Y Richard (2009) Recurrent daily OLR
701 patterns in the Southern Africa/Southwest Indian Ocean region, implications for South
702 African rainfall and teleconnections. Clim Dyn 32:575–591
703 Gelaro R, et al. (2017) The Modern-Era Retrospective Analysis for Research and
704 Applications, Version 2 (MERRA-2). J Clim, doi:10.1175/JCLI-D-16-0758.1
705 Gong X, MB Richman (1995) On the application of cluster analysis to growing season
706 precipitation data in North America East of the Rockies. J Clim 8:897–931
707 Harris I, PD Jones, TJ Osborn, DH Lister (2014) Updated high-resolution grids of monthly
708 climatic observations—The CRU TS3.10 Dataset. Int J Climatol 34:623–642
709 Hart NCG, CJC Reason, N Fauchereau (2010) Tropical–Extratropical Interactions over
710 Southern Africa: Three Cases of Heavy Summer Season Rainfall. Mon Weather Rev
711 138:2608–2623
712 Hermes JC, CJC Reason (2009) Variability in sea-surface temperature and winds in the
713 tropical south-east Atlantic Ocean and regional rainfall relationships. Int J Climatol
714 29(1): 11–21
715 Hoell A, C Funk, T Magadzire, J Zinke, G Husak (2015) El Niño–Southern Oscillation
716 diversity and Southern Africa teleconnections during austral summer. Clim Dyn
717 45:1583–1599
718 Hoell A, C Funk, J Zinke, L Harrison (2017) Modulation of the Southern Africa precipitation
719 response to the El Niño Southern Oscillation by the subtropical Indian Ocean Dipole.
720 Clim Dyn 48:2529–2540

721 Huffman GJ, RF Adler, M Morrissey, DT Bolvin, S Curtis, R Joyce, B McGavock, J
722 Susskind (2001) Global Precipitation at One-Degree Daily Resolution from Multi-
723 Satellite Observations. J Hydrometeor 2:36–50
724 Huffman GJ, DT Bolvin (2012, last updated 19 Feb 2013) Version 1.2 GPCP One-Degree
725 Daily Precipitation Data Set Documentation, NASA Goddard Space Flight Center.
726 https://climatedataguide.ucar.edu/climate-data/gpcp-daily-global-precipitation-
727 climatology-project#sthash.RmP8AHjs.dpuf
728 Kanamitsu M, W Ebisuzaki, J Woollen, SK Yang, J Hnilo, M Fiorino, GL Potter (2002)
729 NCEP-DOE AMIP-2 Reanalysis (R-2). Bull Atmos Meteorol Soc 83:1631–1643
730 Liebmann B, CA Smith (1996) Description of a complete (interpolated) outgoing longwave
731 radiation dataset. Bull Am Meteorol Soc 77:1275–1277
732 Lindesay JA (1988) South African rainfall, the southern oscillation and a southern hemisphere
733 semi-annual cycle. J Climatol 8:17–30
734 Lyon B, SJ Mason (2007) The 1997–98 Summer Rainfall Season in Southern Africa. Part I:
735 Observations. J Clim 20:5134–5148
736 Macron C, B Pohl, Y Richard, M Bessafi (2014) How do Tropical Temperate Troughs Form
737 and Develop over Southern Africa? J Clim 27:1633–1647
738 Michelangeli P, R Vautard, B Legras (1995) Weather regime occurrence and quasi-
739 stationarity. J Atmos Sci 52:1237–1256
740 Mulenga HM (1998) Southern African climatic anomalies, summer rainfall and the Angola
741 low. Dissertation, University of Cape Town, South Africa
742 Munday C, R Washington (2017) Circulation controls on southern African precipitation in
743 coupled models: The role of the Angola Low. J Geophys Res Atmos 122:861–877
744 Pohl B, P Camberlin (2014) A typology for intraseasonal oscillations. Int J Climatol 34:430–
745 445

746 Ratna SB, S Behera, JV Ratnam, K Takahashi, T Yamagata (2013) An index for tropical
747 temperate troughs over southern Africa. Clim Dyn 41:421–441
748 Ratnam JV, SK Behera, Y Masumoto, T Yamagata (2014) Remote effects of El Niño and
749 Modoki events on the austral summer precipitation of Southern Africa. J Clim 27:3802–
750 3815
751 Rayner NA, DE Parker, EB Horton, CK Folland, LV Alexander, DP Rowell, EC Kent, A
752 Kaplan (2003) Global analyses of sea surface temperature, sea ice, and night marine air
753 temperature since the late nineteenth century. J Geophys Res Atm 108,
754 doi:10.1029/2002JD002670
755 Reason CJC, D Jagadheesha (2005) A model investigation of recent ENSO impacts over
756 southern Africa. Meteorol Atmos Phys 89(1–4):181–205
757 Ropelewski CF, MS Halpert (1989) Precipitation patterns associated with the high indices
758 phase of the southern oscillation. J Clim 2:268–284
759 Rouault M (2003) South East tropical Atlantic warm events and southern African rainfall.
760 Geophys Res Lett 30(5), 8009, doi:10.1029/2002GL014840
761 Rouault M, Y Richard (2005) Intensity and spatial extent of droughts in Southern Africa.
762 Geophys Res Lett 32, L15702, doi:10.1029/2005GL022436
763 Saji NH, BN Goswami, PN Vinayachandran, T Yamagata (1999) A dipole mode in the
764 tropical Indian Ocean. Nature 401:360–363
765 Terray P, S Masson, C Prodhomme, MK Roxy, KP Sooraj (2016) Impacts of Indian and
766 Atlantic oceans on ENSO in a comprehensive modeling framework. Clim Dyn 46:2507–
767 2533
768 Todd M, R Washington (1999) Circulation anomalies associated with tropical-temperate
769 troughs in Southern Africa and the south west Indian Ocean. Clim Dyn 15:937–95.

770 Todd M, R Washington, PI Palmer (2004) Water vapour transport associated with tropical-
771 temperate trough systems over southern Africa and the southwest Indian Ocean. Int J
772 Climatol 24:555–568
773 Vigaud N, Y Richard, M Rouault, N Fauchereau (2007) Water vapour transport from the
774 tropical Atlantic and summer rainfall in tropical southern Africa. Clim Dyn 28:113–123
775 Vigaud N, Y Richard, M Rouault, N Fauchereau (2009) Moisture transport between the South
776 Atlantic Ocean and southern Africa: Relationships with summer rainfall and associated
777 dynamics. Clim Dyn 32(1):113–123
778 Vigaud N, B Pohl, J Crétat (2012) Tropical-temperate interactions over southern Africa
779 simulated by a regional climate model. Clim Dyn 39:2895–2916
780 Ward JH (1963) Hierarchical grouping to optimize an objective function. J Am Stat Assoc
781 58:236–244
782 Washington R, M Todd (1999) Tropical-temperate links in southern African and Southwest
783 Indian Ocean satellite-derived daily rainfall. Int J Climatol 19:1601–1616

784 **Table Captions**

785

786 **Table 1** Main differences between the NCEP2, ERA-I and MERRA2 reanalyses used to
787 extract and describe the main regimes of the Angola Low.

788

789 **Table 2** Repartition of the *N*=5285 daily anomalous patterns of 700-hPa vorticity
790 feeding the AHC within regimes A and B and their respective sub-regimes for the three
791 reanalyses.

792

793 **Table 3** Correlation between the seasonal occurrence of the Angola Low regimes and
794 December-January Niño3.4 SST index.

795 **Figure Captions**

796

797 **Figure 1** (a-e) Schematic view of the AHC procedure applied to *N*=5 spatial patterns
798 described by two grid points A and B. Left column shows the spatial patterns in a Cartesian
799 plan. Right column shows the clusters merged according to dissimilarity distances. Colors
800 represent the successive merging along the procedure. See text for details.

801

802 **Figure 2** (a-c) Daily mean 850-hPa vorticity (shadings every 0.1 s^{-1}; negative/positive
803 values for cyclonic/anticyclonic vortex) and wind (vectors, $m.s^{-1}$) over the NDJFM 1980/81–
804 2014/15 period for NCEP2, ERA-I and MERRA2, respectively. (d-f) Same as (a-c) but for
805 700-hPa vorticity and wind. (g-i) Standard deviation of daily 700-hPa vorticity anomalies
806 (shadings every 0.05 s^{-1}). The black box shows the domain used to identify the main Angola
807 Low regimes.

808

809 **Figure 3** (a-c) Dendrogram tree of the *N*=5285 anomalous patterns of daily 700-hPa
810 vorticity (black box in Fig. 2) utilized to feed the AHC for NCEP2, ERA-I and MERRA2,
811 respectively. (d-f) Associated evolution of the accumulated dissimilarity distance for the last
812 10 merges. Letters A and B show the regimes analyzed with a 2-regime partitioning for the
813 three reanalyses. Letters with number show the regimes analyzed with 6/7-regime
814 partitioning.

815

816 **Figure 4** (a-c) Representativeness of each regime for NCEP2, ERA-I and MERRA2,
817 respectively. For each regime, box-and-whisker plots show the spatial correlations between
818 each of its daily 700-hPa vorticity anomalous patterns and its daily mean anomalous pattern.
819 The boxes have lines at the lower quartile, median, and upper quartile values. The whiskers

820 are lines extending from each end of the boxes to show the extent of the range of the data
821 within 1.5 by inter-quartile range from the upper and lower quartiles. Outliers are displayed
822 by a 'plus' sign. Black stars are mean spatial correlations. Red lines give the 95% confidence
823 bound according to the Bravais-Pearson critical values. Red stars show the mean spatial
824 correlation between all daily anomalous patterns of a given AL regime and the daily mean
825 anomalous pattern of the remaining AL regimes.
826
827 **Figure 5** (a-c) Composite mean anomalies in 700-hPa vorticity (shadings every 0.02 s^{-1};
828 negative/positive values for cyclonic/anticyclonic anomalies) and wind (vectors, $m.s^{-1}$)
829 associated with regime A for NCEP2, ERA-I and MERRA2, respectively. Black contours and
830 blue vectors show vorticity and wind anomalies that are significant at the 95% confidence
831 level according to a bootstrap test detailed in section 2.2.4. (d-f) Same as (a-c) but for regime
832 B.
833
834 **Figure 6** Same as Fig. 5 but for rainfall anomalies.
835
836 **Figure 7** (a-c) Vertical-latitude composite mean anomalies in wind vorticity (shadings
837 every 0.025 s^{-1}) zonally averaged in the 12°E–25°E band associated with regime A for
838 NCEP2, ERA-I and MERRA2, respectively. Only significant anomalies at the 95%
839 confidence level according to a bootstrap test are shown. (d-f) Same as (a-c) but for zonal
840 wind anomalies.
841
842 **Figure 8** Same as Fig. 5 but for a 6/7-regime partitioning.
843
844 **Figure 9** Same as Fig. 8 but for rainfall.

845

846 **Figure 10** (a-e) Daily evolution of composite mean anomalies in 700-hPa vorticity
847 (shadings every 0.02 s^{-1}; negative/positive values for cyclonic/anticyclonic anomalies) and
848 wind (vectors, $m.s^{-1}$) during the growing and mature phases of anomalously weak Angola
849 Low, as seen from regime B1 in ERA-I. Daily evolution is shown from 4 days prior to the
850 first day of regime B1 to 4 days after, every 2 days. Negative lags describe the growing stage
851 of the regimes, while positive lags describe their mature phase. See Section 3.3 for details.
852 Significance tested as in Fig. 5. Vorticity anomalies below the 80% confidence level are
853 masked and those at the 95% confidence level are contoured in black. Wind anomalies in gray
854 are not significant. Wind anomalies in pink, light blue and dark blue are significant at the 80,
855 90 and 95% confidence level, respectively. (f-j), (k-o) and (p-t) Same as (a-e) but for
856 anomalously northward, near-climatological and anomalously southward Angola Low, as
857 seen from regimes B2, B3 and A1 in ERA-I, respectively.

858

859 **Figure 11** (a-c) Seasonal occurrence of anomalously weak Angola Low for NCEP2.
860 ERA-I and MERRA2, respectively. Seasonal occurrence is expressed as the fraction (%) of
861 the number of days spent in each regime (Table 2). (d-s) Same as (a-c) but for the remaining
862 Angola Low regimes.

863

864 **Figure 12** (a-c) Synchronous correlation between the seasonal occurrence of anomalously
865 weak Angola Low and seasonal SSTs during the NDJFM 1980/81–2014/15 period for
866 NCEP2, ERA-I and MERRA2, respectively. Significant correlations at the 95% confidence
867 level are contoured in black. (d-s) Same as (a-c) but for the remaining Angola Low regimes.

868

869 **Figure 13** Scatterplot intersecting Niño3.4 SSTs averaged in December-January (x-axis)
870 and the seasonal (NDJFM) SRI (y-axis) over the 1980/81–2012/13 period. Both time-series
871 are standardized so that mean=0 and standard deviation=1. Positive values represent warm
872 SST anomalies in the Niño3.4 region and wet conditions over subtropical southern Africa,
873 and reversely for negative values. The SRI corresponds to the region colored in maroon in the
874 top-right insert. See Section 2.1 for details on the SRI.
875
876 **Figure 14** (a-c) Scatterplot intersecting subtropical southern African rainfall as seen by
877 the SRI (x-axis) and seasonal occurrence of anomalously weak Angola Low (y-axis) over the
878 NDJFM 1980/81–2012/13 period for NCEP2, ERA-I and MERRA2, respectively. (d-s) Same
879 as (a-c) but for the remaining Angola Low regimes. Both time-series are standardized as in
880 Fig. 13. Positive values represent wet rainfall anomalies and above normal occurrence of the
881 Angola Low regimes, and reversely for negative values. Bravais-Pearson correlations between
882 the SRI and the seasonal occurrence of the regimes are labeled on the panels. Stars (*/**/***)
883 show significant correlation at the 90/95/99% confidence level according to the Bravais-
884 Pearson critical value. Red/Blue colors show associated warm/cold December-January SST
885 anomalies of the Niño3.4 region. The 1982/83 and 1997/98 years taken as case study in
886 Section 4.3 are shown with a 'plus' sign.
887
888 **Figure 15** (a) NDJFM SST climatology for the 1980/81–2014/15 HadISST data. (b)
889 NDJFM SST anomalies in 1982/83 computed as departure from the NDJFM climatology. (c)
890 Same as (b) but for NDJFM 1997/98. (d) Daily mean 200-hPa velocity potential (shadings
891 every $1x10^6$ $m^2.s^{-1}$; negative/positive values for upper-level divergence/convergence) and
892 850-hPa wind (vectors: $m.s^{-1}$) over the NDJFM 1980/81–2014/15 period for ERA-I. (e)
893 Composite anomalies in 200-hPa velocity potential (shadings every $0.8x10^6$ $m^2.s^{-1}$;

894 negative/positive values for upper-level divergence/convergence anomalies) and 850-hPa
895 wind during the NDJFM 1982/83 season. Significance is tested at the 95% confidence level
896 according to a Student t test and shown with black contours for 200-hPa velocity potential
897 anomalies and with black vectors for 850-hPa wind anomalies. (f) Same as (e) but for the
898 NDJFM 1997/98 season.
899
900 **Figure S1** (a) Composite mean anomalies in 700-hPa vorticity (shadings every 0.02 s^{-1};
901 negative/positive values for cyclonic/anticyclonic anomalies) and wind (vectors, $m.s^{-1}$)
902 associated with the six main regimes derived from clustering of ERA-I daily surface pressure
903 anomalies of the 5°-20°S–12°-25°E region. (b) Same as (a) but for rainfall. Black contours
904 and blue vectors show vorticity and wind anomalies that are significant at the 95% confidence
905 level according to a bootstrap test detailed in section 2.2.4. (d-f) Same as (a-c) but the six
906 main regimes derived from clustering analysis of daily 700-hPa geopotential height
907 anomalies.
908
909 **Figure S2** Same as Fig. S1 but for the mean anomalous circulation patterns associated
910 with the six main regimes derived from clustering of ERA-I daily vorticity anomalies at the
911 (a) 600-hPa, (b) 700-hPa and (c) 775-hPa. The vertical level retained in this study is 700-hPa
912 (panel b).
913
914 **Figure S3** Same as Fig. S2 but for rainfall.
915
916
917 **Figure S4** Same as Fig. S1 but for the mean anomalous circulation patterns associated
918 with the six main regimes derived from clustering of ERA-I daily 700-hPa vorticity anomalies

over the (a) 5-20°S 12-25°E, (b) 4-21°S 11-26°E, (c) 3-22°S 10-27°E, (d) 2-23°S 9-28°E, (e) 1-24°S 8-29°E and (f) Eq-25°S 7-30°E domains. The domain retained in this study is 5-20°S 12-25°E (panel a).

Figure S5 Same as Fig. S4 but for rainfall.

Figure S6 Same as Fig. 7a-c but for a 6/7-regime partitioning.

Tables

Table 1 Main differences between the NCEP2, ERA-I and MERRA2 reanalyses used to extract and describe the main regimes of the Angola Low.

	Resolution		Atmospheric Model	Assimilation technique	SST & sea-ice forcing
	Horizontal	Vertical			
NCEP2	2.5° x 2.5°	28	Climate Forecast System (CFS)	3 Dimensional Variational (3DVAR)	Weekly Optimum Interpolation Sea Surface Temperature (OISST)
ERA-I	0.75° x 0.75°	60	Integrated Forecasting System (IFS)	4DVAR	Daily OISST
MERRA2	0.5° x 0.625°	72	Goddard Earth Observing System version 5 (GEOS-5)	3DVAR	Weekly OISST

Table 2 Repartition of the *N*=5285 daily anomalous patterns of 700-hPa vorticity feeding the AHC within regimes A and B and their respective sub-regimes for the three reanalyses.

	NCEP2	**ERA-I**	**MERRA2**
Regime A	**3151**	**1149**	**3149**
A1	1684	602	529
A2	561	547	636
A3	458	/	1406
A4	448	/	281
A5	/	/	297
Regime B	**2134**	**4136**	**2136**
B1	1904	1073	1399
B2	230	490	737
B3	/	1610	/
B4	/	963	/

Table 3 Correlation between the seasonal occurrence of the Angola Low regimes and December-January Niño3.4 SST index.

	NCEP2	**ERA-I**	**MERRA2**
Weak AL	+0.25 (B1)	+0.41** (B1)	+0.44** (B1)
Northward AL	-0.12 (B2)	+0.05 (B2)	+0.29* (B2)
Near-climatological AL	-0.29* (A1) +0.36** (A2)	+0.02 (B3) +0.09 (B4)	-0.44** (A1) +0.25 (A2)
Southward AL	-0.25 (A3) -0.29* (A4)	-0.30* (A1) -0.49** (A2)	-0.35** (A3) -0.37** (A4) -0.29* (A5)

* and ** show correlation values that are significant at the 90% and 95% confidence level according to the Bravais-Pearson critical value.

947 **Figures**
948
949

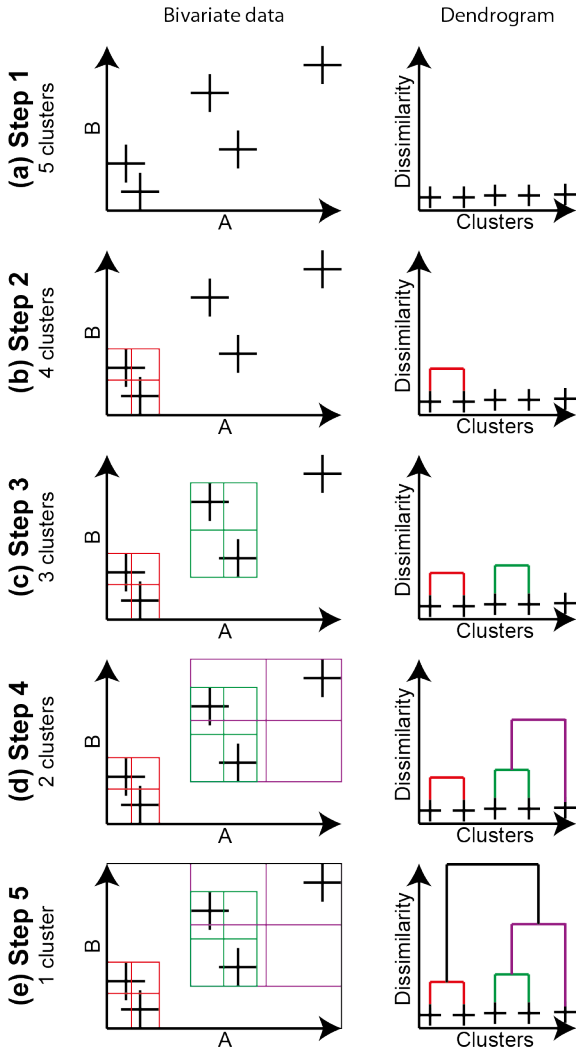

950
951
952 **Figure 1** (a-e) Schematic view of the AHC procedure applied to *N*=5 spatial patterns described by two
953 grid points A and B. Left column shows the spatial patterns in a Cartesian plan. Right column shows the clusters
954 merged according to dissimilarity distances. Colors represent the successive merging along the procedure. See
955 text for details.

Figure 2 (a-c) Daily mean 850-hPa vorticity (shadings every 0.1 s^{-1}; negative/positive values for cyclonic/anticyclonic vortex) and wind (vectors, $m.s^{-1}$) over the NDJFM 1980/81–2014/15 period for NCEP2, ERA-I and MERRA2, respectively. (d-f) Same as (a-c) but for 700-hPa vorticity and wind. (g-i) Standard deviation of daily 700-hPa vorticity anomalies (shadings every 0.05 s^{-1}). The black box shows the domain used to identify the main Angola Low regimes.

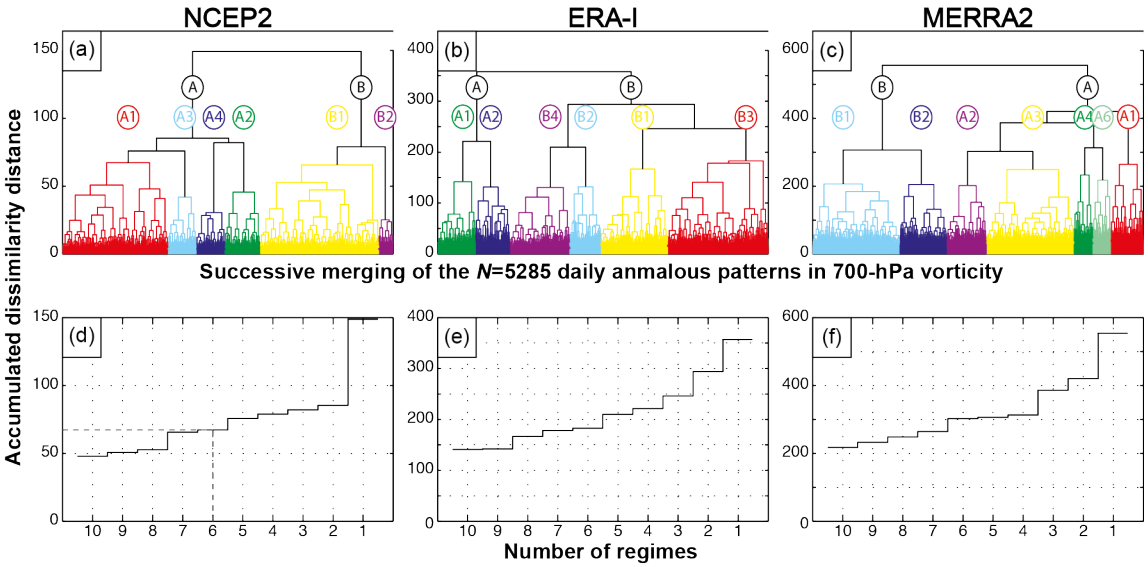

Figure 3 (a-c) Dendrogram tree of the *N*=5285 anomalous patterns of daily 700-hPa vorticity (black box in Fig. 2) utilized to feed the AHC for NCEP2, ERA-I and MERRA2, respectively. (d-f) Associated evolution of the accumulated dissimilarity distance for the last 10 merges. Letters A and B show the regimes analyzed with a 2-regime partitioning for the three reanalyses. Letters with number show the regimes analyzed with 6/7-regime partitioning.

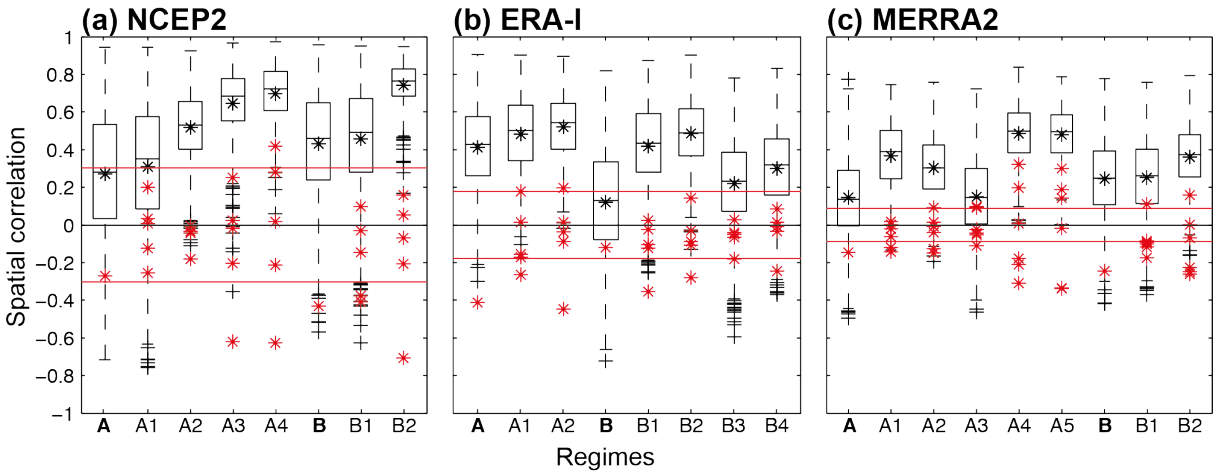

Figure 4 (a-c) Representativeness of each regime for NCEP2, ERA-I and MERRA2, respectively. For each regime, box-and-whisker plots show the spatial correlations between each of its daily 700-hPa vorticity anomalous patterns and its daily mean anomalous pattern. The boxes have lines at the lower quartile, median, and upper quartile values. The whiskers are lines extending from each end of the boxes to show the extent of the range of the data within 1.5 by inter-quartile range from the upper and lower quartiles. Outliers are displayed by a 'plus' sign. Black stars are mean spatial correlations. Red lines give the 95% confidence bound according to the Bravais-Pearson critical values. Red stars show the mean spatial correlation between all daily anomalous patterns of a given AL regime and the daily mean anomalous pattern of the remaining AL regimes.

Figure 5 (a-c) Composite mean anomalies in 700-hPa vorticity (shadings every 0.02 s^{-1}; negative/positive values for cyclonic/anticyclonic anomalies) and wind (vectors, $m.s^{-1}$) associated with regime A for NCEP2, ERA-I and MERRA2, respectively. Black contours and blue vectors show vorticity and wind anomalies that are significant at the 95% confidence level according to a bootstrap test detailed in Section 2.2.4. (d-f) Same as (a-c) but for regime B.

988
989
990 **Figure 6** Same as Fig. 5 but for rainfall anomalies.

991
992
993 **Figure 7** (a-c) Vertical-latitude composite mean anomalies in wind vorticity (shadings every 0.025 s^{-1})
994 zonally averaged in the 12°E–25°E band associated with regime A for NCEP2, ERA-I and MERRA2,
995 respectively. Only significant anomalies at the 95% confidence level according to a bootstrap test are shown. (d-
996 f) Same as (a-c) but for zonal wind anomalies.

997
998
999 **Figure 8** Same as Fig. 5 but for a 6/7-regime partitioning.

1000
1001
1002 **Figure 9** Same as Fig. 8 but for rainfall.

Figure 10 (a-e) Daily evolution of composite mean anomalies in 700-hPa vorticity (shadings every 0.02 s^{-1}; negative/positive values for cyclonic/anticyclonic anomalies) and wind (vectors, $m.s^{-1}$) during the growing and mature phases of anomalously weak Angola Low, as seen from regime B1 in ERA-I. Daily evolution is shown from 4 days prior to the first day of regime B1 to 4 days after, every 2 days. Negative lags describe the growing stage of the regimes, while positive lags describe their mature phase. See Section 3.3 for details. Significance tested as in Fig. 5. Vorticity anomalies below the 80% confidence level are masked and those at the 95% confidence level are contoured in black. Wind anomalies in gray are not significant. Wind anomalies in pink, light blue and dark blue are significant at the 80, 90 and 95% confidence level, respectively. (f-j), (k-o) and (p-t) Same as (a-e) but for anomalously northward, near-climatological and anomalously southward Angola Low, as seen from regimes B2, B3 and A1 in ERA-I, respectively.

1015
1016
1017 **Figure 11** (a-c) Seasonal occurrence of anomalously weak Angola Low for NCEP2. ERA-I and
1018 MERRA2, respectively. Seasonal occurrence is expressed as the fraction (%) of the number of days spent in
1019 each regime (Table 2). (d-s) Same as (a-c) but for the remaining Angola Low regimes.

1020
1021
1022 **Figure 12** (a-c) Synchronous correlation between the seasonal occurrence of anomalously weak Angola
1023 Low and seasonal SSTs during the NDJFM 1980/81–2014/15 period for NCEP2, ERA-I and MERRA2,
1024 respectively. Significant correlations at the 95% confidence level are contoured in black. (d-s) Same as (a-c) but
1025 for the remaining Angola Low regimes.

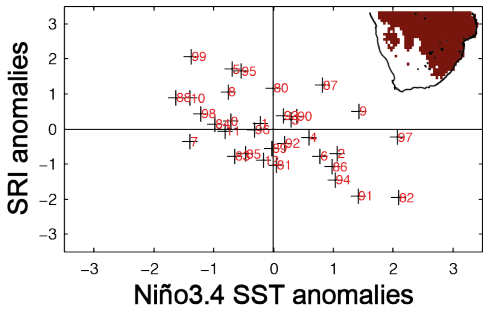

Figure 13 Scatterplot intersecting Niño3.4 SSTs averaged in December-January (x-axis) and the seasonal (NDJFM) SRI (y-axis) over the 1980/81–2012/13 period. Both time-series are standardized so that mean=0 and standard deviation=1. Positive values represent warm SST anomalies in the Niño3.4 region and wet conditions over subtropical southern Africa, and reversely for negative values. The SRI corresponds to the region colored in maroon in the top-right insert. See Section 2.1 for details on the SRI.

Figure 14 (a-c) Scatterplot intersecting subtropical southern African rainfall as seen by the SRI (x-axis) and seasonal occurrence of anomalously weak Angola Low (y-axis) over the NDJFM 1980/81–2012/13 period for NCEP2, ERA-I and MERRA2, respectively. (d-s) Same as (a-c) but for the remaining Angola Low regimes. Both time-series are standardized as in Fig. 13. Positive values represent wet rainfall anomalies and above normal occurrence of the Angola Low regimes, and reversely for negative values. Bravais-Pearson correlations between the SRI and the seasonal occurrence of the regimes are labeled on the panels. Stars (*/**/***) show significant correlation at the 90/95/99% confidence level according to the Bravais-Pearson critical value. Red/Blue colors show associated warm/cold December-January SST anomalies of the Niño3.4 region. The 1982/83 and 1997/98 years taken as case study in Section 4.3 are shown with a 'plus' sign.

Figure 15 (a) NDJFM SST climatology for the 1980/81–2014/15 HadISST data. (b) NDJFM SST anomalies in 1982/83 computed as departure from the NDJFM climatology. (c) Same as (b) but for NDJFM 1997/98. (d) Daily mean 200-hPa velocity potential (shadings every 1x106 m2.s-1; negative/positive values for upper-level divergence/convergence) and 850-hPa wind (vectors: m.s-1) over the NDJFM 1980/81–2014/15 period for ERA-I. (e) Composite anomalies in 200-hPa velocity potential (shadings every 0.8x106 m2.s-1; negative/positive values for upper-level divergence/convergence anomalies) and 850-hPa wind during the NDJFM 1982/83 season. Significance is tested at the 95% confidence level according to a Student t test and shown with black contours for 200-hPa velocity potential anomalies and with black vectors for 850-hPa wind anomalies. (f) Same as (e) but for the NDJFM 1997/98 season.

Supplementary material

Figure S1 (a) Composite mean anomalies in 700-hPa vorticity (shadings every 0.02 s^{-1}; negative/positive values for cyclonic/anticyclonic anomalies) and wind (vectors, $m.s^{-1}$) associated with the six main regimes derived from clustering of ERA-I daily surface pressure anomalies of the 5°-20°S–12°-25°E region. (b) Same as (a) but for rainfall. Black contours and blue vectors show vorticity and wind anomalies that are significant at the 95% confidence level according to a bootstrap test detailed in section 2.2.4. (d-f) Same as (a-c) but the six main regimes derived from clustering analysis of daily 700-hPa geopotential height anomalies.

Figure S2 Same as Fig. S1 but for the mean anomalous circulation patterns associated with the six main regimes derived from clustering of ERA-I daily vorticity anomalies at the (a) 600-hPa, (b) 700-hPa and (c) 775-hPa. The vertical level retained in this study is 700-hPa (panel b).

Figure S3 Same as Fig. S2 but for rainfall.

Figure S4 Same as Fig. S1 but for the mean anomalous circulation patterns associated with the six main regimes derived from clustering of ERA-I daily 700-hPa vorticity anomalies over the (a) 5-20°S 12-25°E, (b) 4-21°S 11-26°E, (c) 3-22°S 10-27°E, (d) 2-23°S 9-28°E, (e) 1-24°S 8-29°E and (f) Eq-25°S 7-30°E domains. The domain retained in this study is 5-20°S 12-25°E (panel a).

Figure S5 Same as Fig. S4 but for rainfall.

Figure S6 Same as Fig. 7a-c but for a 6/7-regime partitioning.